The Astrophysical Journal, 768:121 (15pp), 2013 May 10 doi:10.1088/0004-637X/768/2/121

HST SPECTRAL MAPPING OF L/T TRANSITION BROWN DWARFS REVEALS CLOUD THICKNESS VARIATIONS

Dániel Apai[1,6], Jacqueline Radigan[2,7], Esther Buenzli[3], Adam Burrows[4], Iain Neill Reid[5], and Ray Jayawardhana[2]
[1] Department of Astronomy, The University of Arizona, 933 N. Cherry Avenue, Tucson, AZ 85721, USA; apai@as.arizona.edu
[2] Department of Astronomy, University of Toronto, 50 St. George Street, Toronto M5S 3H4, Canada
[3] Department of Astronomy and Steward Observatory, 933 N. Cherry Avenue, The University of Arizona, Tucson, AZ 85721, USA
[4] Department of Astrophysical Sciences, 105 Peyton Hall, Princeton University, Princeton, NJ 08544, USA
[5] Space Telescope Science Institute, 3700 San Martin Drive, Baltimore, MD 21212, USA
Received 2012 September 25; accepted 2013 March 13; published 2013 April 22

ABSTRACT

Most directly imaged giant exoplanets are fainter than brown dwarfs with similar spectra. To explain their relative underluminosity, unusually cloudy atmospheres have been proposed. However, with multiple parameters varying between any two objects, it remained difficult to observationally test this idea. We present a new method, sensitive time-resolved *Hubble Space Telescope* near-infrared spectroscopy, to study two rotating L/T transition brown dwarfs (2M2139 and SIMP0136). The observations provide spatially and spectrally resolved mapping of the cloud decks of the brown dwarfs. The data allow the study of cloud structure variations while other parameters are unchanged. We find that both brown dwarfs display variations of identical nature: *J*- and *H*-band brightness variations with minimal color and spectral changes. Our light curve models show that even the simplest surface brightness distributions require at least three elliptical spots. We show that for each source the spectral changes can be reproduced with a linear combination of only two different spectra, i.e., the entire surface is covered by two distinct types of regions. Modeling the color changes and spectral variations together reveal patchy cloud covers consisting of a spatially heterogeneous mix of low-brightness, low-temperature thick clouds and brighter, thin, and warm clouds. We show that the same thick cloud patches seen in our varying brown dwarf targets, if extended to the entire photosphere, predict near-infrared colors/magnitudes matching the range occupied by the directly imaged exoplanets that are cooler and less luminous than brown dwarfs with similar spectral types. This supports the models in which thick clouds are responsible for the near-infrared properties of these "underluminous" exoplanets.

Key words: brown dwarfs – planetary systems – planets and satellites: individual (Jupiter) – stars: atmospheres – stars: low-mass – starspots

Online-only material: color figures

1. INTRODUCTION

With masses between cool stars and giant exoplanets and effective temperatures comparable to those of directly imaged exoplanets (e.g., Chauvin et al. 2005; Marois et al. 2008; Lafrenière et al. 2008; Marois et al. 2010; Lagrange et al. 2010; Skemer et al. 2011) L- and T-type brown dwarfs provide the critical reference points for understanding the atmospheres of exoplanets (e.g., Burrows et al. 2001; Kirkpatrick 2005; Marley et al. 2007). Because the observations of brown dwarfs are not limited by the extreme star-to-planet contrasts exoplanet observations pose, much more detailed studies can be carried out. In particular, brown dwarfs provide an opportunity to solve the puzzling observation that most directly imaged giant planets appear to be redder and up to 4–10 times fainter than typical brown dwarfs with the same spectral type (e.g., Barman et al. 2011a; Skemer et al. 2012), often referred to as the *underluminosity problem*. Particularly interesting well-studied examples are seen in Ross 458C (Burgasser et al. 2010; Burningham et al. 2011; Morley et al. 2012) and 2M1207b (Chauvin et al. 2005; Mohanty et al. 2007; Patience et al. 2010; Barman et al. 2011b; Skemer et al. 2011). Although for the case of 2M1207b an obscuring edge-on disk with gray extinction has been proposed as a solution, in light of additional observations and analysis this solution appears very unlikely (Skemer et al. 2011). More likely is that the fainter and redder near-infrared emission is due to a property intrinsic to the atmospheres of these exoplanets. This possibility is further supported by the fact that similar underluminosity has also been reported for a handful of field brown dwarfs (e.g., HD 203030B: Metchev & Hillenbrand 2006, HN Peg B: Luhman et al. 2007, 2MASSJ18212815+1414010, 2MASSJ21481628+4003593: Looper et al. 2008) and young brown dwarfs in clusters (Lucas et al. 2001; Allers et al. 2006). The different models proposed to explain the lower near-infrared luminosity of exoplanets and brown dwarfs invoke differences in elemental abundances, surface gravity differences, evolutionary state, chemical equilibrium/non-equilibrium, or cloud structure, or some combination of these. However, because several of these parameters may change between any two brown dwarfs or exoplanets it remained difficult to isolate the effect of these variables. Possible differences in the structure of condensate clouds have, in particular, received much attention in models (e.g., Ackerman & Marley 2001; Burgasser et al. 2002; Skemer et al. 2012; Barman et al. 2011a, 2011b; Burrows et al. 2006; Madhusudhan et al. 2011; Marley et al. 2010) and progress has been made in spectroscopic modeling to separate or constrain the impact of cloud structure from other parameters (e.g., Cruz et al. 2007; Folkes et al. 2007; Looper et al. 2008; Burgasser et al. 2008; Radigan et al. 2008; Cushing et al. 2010). Yet, this problem remains a challenging aspect of ultracool atmospheres

[6] Also at Department of Planetary Sciences, 1629 E. University Blvd, Tucson, AZ 85721, USA.
[7] Also at Space Telescope Science Institute, 3700 San Martin Drive, Baltimore, MD 21212, USA.

Table 1
Log of Observations and Noise Measurements

Target Name	Date	Time Per Int.	No. of Int. /Orbit	No. of Orbits	Total No. of Spectra	Bin Size	Noise per Int.
2M2139	2010 Oct 21	22.34 s	11	6	660	10	0.27%
SIMP0136	2011 Oct 10	22.34 s	16 or 17	6	495	5	0.11%

and one which will benefit from observational data probing cloud properties more directly.

We present here high-cadence, high-precision, time-resolved *Hubble Space Telescope* (*HST*) spectroscopy of two rotating early T-type brown dwarfs that reveal highly heterogeneous cloud covers across their photospheres. These observations allow us to separate the effects of different cloud structures from variations in surface gravity, elemental abundances, age, and evolutionary state. We show that the observed variations are well reproduced by models with large cloud scale height variations (thin and thick clouds) across the surfaces. When thick clouds turn to the visible hemispheres both targets fade in the near-infrared and display changes consistent with the colors and brightness of underluminous directly imaged exoplanets. The similarity of the changes observed provides strong support to models that invoke atmospheres with high dust scale heights to explain the photometry of directly imaged exoplanets.

2. OBSERVATIONS AND DATA REDUCTION

2.1. Observations and Targets

We used the *HST* to obtain near-infrared grism spectroscopy of two L/T transition brown dwarfs as part of a larger campaign (Programs 12314, 12551 PI: Apai). The data were acquired with the sensitive Wide-Field Camera 3 instrument (MacKenty et al. 2010) by obtaining 256×256 pixel images of the targets' spectra dispersed by the G141 grism in six consecutive *HST* orbits. Table 1 provides a log of the observations. In short, we obtained 660 spectra for 2M2139, each with 22.34 s integration time; and 495 spectra for SIMP0136, each with 22.34 s integration time. In the analysis that follows we averaged sets of 10 spectra for 2M2139 and sets of 5 spectra for SIMP0136, giving us an effective temporal resolution of 223 s for 2M2139 and 112 s for SIMP0136. Our targets are relatively bright ($J = 13.5$ mag for SIMP0136 and $J = 15.3$ mag for 2M2139), resulting in very high signal-to-noise spectra (see Section 2.3 for a detailed assessment).

At the beginning of each orbit a direct image was obtained to accurately determine the position of the source on the detector, required for precise wavelength calibration. Cross-correlation of the images and centroid positions on source revealed positional differences less than 0.1 pixel (0.″01) between images taken at different orbits. No dithering was applied to stabilize source positions and improve the accuracy of relative measurements.

The observations presented here focus on two L/T transition brown dwarfs. Target 2M2139 (or 2MASS J21392676+0220226) has been classified as a T0 dwarf based on red optical spectrum (Reid et al. 2008) and as a peculiar T2.5 ± 1 dwarf based on a 0.8–2.5 μm spectrum (Burgasser et al. 2006). More recently, Burgasser et al. (2010) found that the spectrum of 2M2139 is better fit by a composite spectrum of an earlier- (L8.5) and a later-type (T3.5) dwarf than any single template brown dwarf. It was recently found to show impressive periodic photometric variability with a peak-to-peak amplitude of $\simeq$27% (Radigan et al. 2012). Ground-based photometry of variation 2M2139 argues for a period of 7.721 ± 0.005 hr, but also leaves open the possibility of a two times longer period (Radigan et al. 2012). Recent observations by Khandrika et al. (2013) confirm the variability and argue against a double-peak period. Based on *JHK* light curves and a fit to the spectrum by Burgasser et al. (2006), these authors argue that cloud thickness variations are likely responsible for the photometric variations seen in 2M2139. Target SIMP0136 (2MASS J0136565+093347), another T2 brown dwarf, has also been reported variable (Artigau et al. 2009). These targets are the first L/T transition sources observed in our two ongoing *HST* surveys; further results, including coordinated *HST*/*Spitzer* observations and sources with later spectral types, are discussed in Buenzli et al. (2012) and other upcoming papers.

2.2. Data Reduction

Our reduction pipeline combined the standard aXe pipeline with a custom-made IDL script, which included corrections for different low-level detector systematics, critical for highly precise relative spectroscopy. We used two-dimensional spectral images from the standard WFC3 pipeline, which were bias and dark current-subtracted, and corrected for non-linearity and gain. Bad pixels were marked by a corresponding flag in the data quality plane. In order to correct for detector systematics we started with the `.ima` files, which contain all non-destructive sub-reads of each exposure, rather than the combined `.flt` images. Because our observations were not taken with a dithering pattern, we did not use the standard pipeline's `MultiDrizzle` routine.

We first extracted all sub-reads, discarded the first two zero-reads (0 s and 0.27 s), and compared the count rates of the individual pixels over the sub-reads of an exposure to identify and remove outliers by replacing them with the median value. We also corrected flagged bad pixels by interpolating over adjacent good pixels in the same row.

We identified a systematic nearly linear flux loss from the first to last sub-read of an exposure, with a steeper slope for the brighter pixels of a spectrum. We empirically determined a slope of −0.2% per 22.34 s (one sub-read) for pixels of brightness >60% of the maximum in the spectrum, and only −0.001% for pixels below that level (Figure 1). The uncertainties of the slopes are negligible, but a significant "zig-zag" pattern is present with a scatter of ∼0.1%. The standard deviation of the normalized fluxes measured at the same exposure but in different orbits is $\leqslant$0.2%. This relation held for all of our objects, regardless of the absolute brightness of the spectra. Only the first sub-read had systematically higher flux than expected from the linear relation and had to be corrected individually for each source.

The spectral extraction was executed with aXe (Space Telescope-European Coordinating Facility, ESA 2011). First, the sub-array images were embedded in larger, full frame-sized images to allow aXe to use standard instrument calibration frames, which are full frame sized. The data quality flag was used to exclude the extra surrounding pixels of the extended frame from the actual data analysis. As a first step, the aXe pipeline

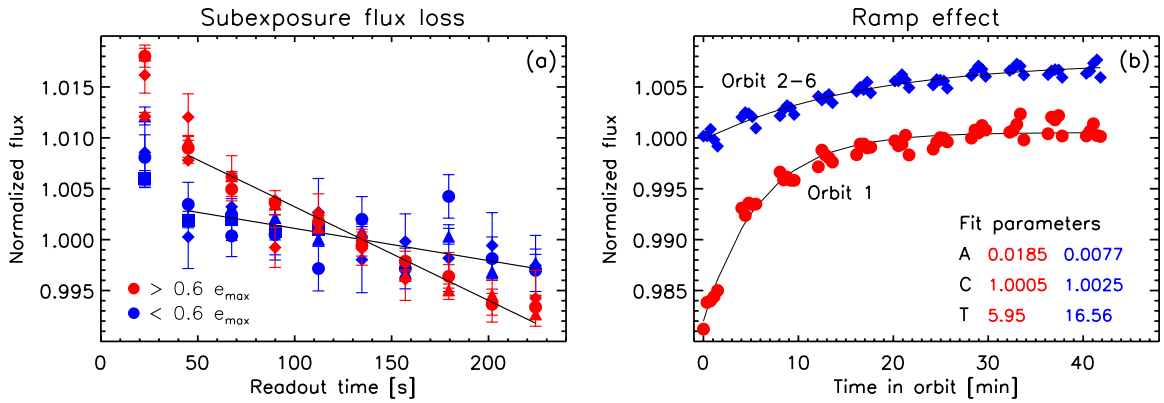

Figure 1. Systematic effects observed and corrected in the WFC3 data: flux loss (a) and ramp (b). Both effects are well fitted and removed by simple analytical functions. In (a), sources are shown with counts <0.6 (blue) or >0.6 (red) of the maximum count in the spectrum. In (b), blue symbols are ramp in orbits 2–6 and red symbols are the ramp in orbit 1. Here, the source is a non-variable field star.

(A color version of this figure is available in the online journal.)

subtracted a scaled master sky frame, with the scale factor determined individually for each images background level (i.e., excluding the observed spectra). Then, the location of the target spectrum and the wavelength calibration were determined from the direct (non-grism) images. For the source 2M2139, only one direct image was obtained at the beginning of the first orbit and this image was used for each subsequent spectra. For SIMP0136, a separate direct image was taken at the beginning of each orbit and used for all spectra in the given orbit. We fixed the spectral extraction width within each orbit, but allowed it to vary between subsequent orbits. The extraction width was determined by summing up all spectra in a single orbit and then collapsing the sum into a one-dimensional (1D) vertical profile. The extraction width was then chosen as three times the full width at half-maximum of a Gaussian fit to that profile. This resulted in an extraction width with mean and standard deviation for the six orbits of 6.50 ± 0.02 for SIMP0136 and 6.56 ± 0.01 pixels for 2M2139, respectively.

In the final step the spectra from each image were flat fielded, extracted, and collapsed using the standard pixel extraction tables of aXe and flux-calibrated with the latest instrument sensitivity curves. This led to 1D spectra with a spectral resolution of $R = \lambda/\Delta\lambda \simeq 130$ and highly reliable data over the wavelength range from 1.1 to 1.7 μm. We calculated the uncertainties as composed of photon shot noise, read noise, and sky noise. A second systematic detector effect became evident at this point. During each orbit, there was a small increase in flux in the form of an exponential ramp (Figure 1). Because the intrinsic variability of the sources prevented a direct quantification of this effect, we used the partial spectrum of a bright star visible in one of our target fields. The ramp was found to be independent of object brightness. We integrated the stellar spectrum over the full wavelength range and removed exposures where saturation had occurred. We fitted the exponential ramp $C \times (1 - Ae^{-t/T})$ to the light curve, where t is the time since the beginning of an orbit. The ramp was very similar for all the orbits between the second and sixth, which we therefore averaged before fitting, but it was a different, stronger effect in the first orbit of a visit, which was fitted and corrected individually. In the final step, we corrected the spectra of all our objects by dividing the time-dependent data by the value of the analytical ramp function sampled at the times of the subreads. Figure 1 shows the ramp and its best-fit parameters. The latter are the following: for orbit 1: $A = 0.0185 \pm 0.0013$, $T = 5.95 \pm 0.88$, and $C = 1.0005 \pm 0.0005$, while for orbits 2–6: $A = 0.0077 \pm 0.0009$, $T = 16.65 \pm 6.02$, and $C = 1.0025 \pm 0.0009$. Note that these uncertainties include the propagated uncertainties from the slope correction described above. The combined uncertainties for the ramp correction lead to a 1σ uncertainty of $\simeq$0.15%.

2.3. Uncertainties

In the following, we briefly discuss the uncertainties of our measurements. We distinguish three different uncertainties that affect our data: random (white) noise emerging from photon noise and readout noise, systematic wavelength-dependent trends, and systematic time-dependent trends. As explained below, due to the fact that our targets are very bright by *HST*'s standards the photon noise is very small (typically well below 0.1%) and the systematic wavelength-dependent trends are negligible, the residual time-dependent trends dominate the noise in our data. We characterize the amplitude of each of these three components based on our data.

2.3.1. White Noise

Random (white) noise is present in our data due to the combination of photon noise, residual dark noise, and readout noise. While all three components are present at very low levels, often negligible for practical purposes, we use our data to measure their combined amplitude. To do this we extract pixel-to-pixel variations helped by the fact that our temporal resolution (<1 minute) significantly exceeds the timescale on which the astrophysical changes occur. We started from the binned spectral cubes containing 66 spectra (each with 10 binned readouts) for 2M2139 and 99 spectra (each with 5 binned samples) for SIMP0136. To measure the white noise we removed the correlated components by first subtracting a two-pixel-smoothed version of the data, leaving only variations smaller than two resolution elements. In the low-resolution *HST* data, most of the changes even on this small scale are correlated physical changes (i.e., high-frequency residuals of actual spectral features). These features are the same in every spectra and can be removed via the subtraction of the median spectrum of the spectral cube. This procedure has removed correlated changes in wavelength and in time, leaving us with white noise-dominated data. To measure the white noise amplitude, we calculated the standard deviation of the data in

each spectrum and their median. We find that for 2M2139 the 1σ noise per resolution element is 0.27%, while for the brighter SIMP0136 the 1σ noise per resolution elements is 0.11%.

We point out that most of the conclusions in this paper are drawn from brightness variations measured in broad photometric bands, further decreasing the importance of white noise. For example, the *J*-band light curves in our spectra typically contain 55 data points, leading to a white noise contribution of less than 0.04%.

2.3.2. Time-dependent Trends

Because we study temporal changes in our targets it is important to assess the level of time-dependent trends (red noise) in our data. Any red noise present in the data would come from time-dependent sensitivity variations, potentially introduced either by drifts in the positions of the sources or by sensitivity changes in the instrument. Our measurements of the positions of the sources show that the targets have remained in precisely the same positions, thus contribution from the former noise factor cannot be significant. The second noise source, changes in the instrumental sensitivity, however, must be characterized through our data. Due to observing efficiency considerations, our observations were taken in a sub-array mode, which has a relatively small field of view and thus do not contain any other sources of comparable brightness to the targets. Therefore, we do not have other non-varying sources in the same data sets that could be used to measure time-dependent trends in our data. Instead, we use a third brown dwarf target observed identically to our targets to assess time-dependent trends. This third target, 2MASSJ09153413+0422045 (in the following 2M0915), did not show variability above the 0.6% level and thus provides us with a good reference for measuring the temporal stability of the observations. 2M0915 is a resolved binary brown dwarf (L7+L7; Reid et al. 2006), allowing us to measure flux levels for the two sources simultaneously. We point out that although the wings of the two spectra show some overlap, this overlap should not affect the photometric stability of the measurements and the following assessment of the systematic uncertainties.

We reduced the 2M0915 data set in the same way as data from the other two sources, with the exception that a larger aperture was adopted to include both of the slightly overlapping sources. The data reduction was repeated two times, with the aperture once centered on component A and once centered on component B.

For the two components we measured a mean standard deviation of points *within* the same orbit of 0.16% and 0.13%, fully consistent with the combined uncertainties of the correction of the systematic effects and the white noise components. The fact that this standard deviation is not larger demonstrates that there is no measurable systematic trend left uncorrected on timescales of an orbit or less.

To assess the photometric stability of *HST* over timescales of multiple orbits we determined the scatter of the mean values in each orbit. Thus, we calculated the standard deviation of the mean values of the fluxes measured in each of the six orbits. We found that these values were 0.25% and 0.13% for the two components; these values are our estimates for the uncertainties of the photometric stability of *HST* over six orbits.

Thus, based on the measurements of the noise properties we conclude the following: (1) the random (white) noise level is 0.3% per resolution element and integration, (2) the random noise of band-integrated light curves is less than 0.04% (practically negligible), (3) the photometric stability between orbits is about 0.25% or less, and (4) photometric trends within an orbit (<50 minutes) amount to 0.16% or less. Therefore, although the differences discussed in our paper are small (typically few percent levels) they are all high significance level detections.

3. RESULTS

Our observations provided a series of very high signal-to-noise (S/N > 300) spectra (see Figure 2) of the targets covering the 1.1–1.7 μm wavelength range. These spectra probe the *J* and *H* broadband photometric bands, prominent molecular absorption bands (water and methane), as well as atomic resonance lines (K I and Na I).

The spectra of both targets are dominated by deep and broad water vapor absorption at 1.1 μm, 1.4 μm, and 1.7 μm. Characteristic of L/T transition dwarfs, they both display narrower neutral atomic lines and weaker CH_4 absorption. Both sources showed dramatic brightness changes during the observations. Synthetic photometry derived in the core of the standard *J* and *H* bands (centered at 1.2 and 1.6 μm) display variations with peak-to-peak amplitudes of 27% (2M2139) and 4.5% (SIMP0136). The variations are periodic and we estimate the periods to be 7.83 ± 0.1 hr and 2.39 ± 0.05 hr for 2M2139 and SIMP0136, respectively. The period for 2M2139 was derived by least-squares minimization of the light curve segments overlapping in phase (see inset in Figure 2) and leads to a 0.35% standard deviation in the overlapping region, but a slightly imperfect match in light curve shape. In contrast, a somewhat shorter period (7.76 hr) provides a near-perfect match for the light curve shape, but leads to a slightly higher standard deviation (0.55%). Given the information at hand, we conservatively assume that the period is 7.83 ± 0.1 hr. Determining the period for SIMP0136 poses a different challenge: although the overlap in phase is much larger than it is for 2M2139, the light curve shows a clear evolution during the extent of our observations. We find that assuming a period of 2.39 hr aligns the troughs in the light curve, but leads to a shift between consecutive peaks; in turn, a period of 2.42 hr aligns the peaks well but leads to a mismatch in the troughs. This behavior is fully consistent with the light curve evolution observed in this source; in the following we conservatively assume that the period of SIMP0136 is 2.39 ± 0.07 hr.

These rotational periods were determined by minimizing the differences in phase-folded light curves. The periods are consistent with those reported for these sources from ground-based photometry (Radigan et al. 2012; Artigau et al. 2009). For 2M2139 our first and sixth *HST* orbits cover the same phase for an assumed period of 7.83 hr. During this overlap the spectra and the flux levels provide very close match in the shape of the light curve. The flux levels differ by only 0.5%, which is twice the 1σ uncertainty we estimated for the photometric stability of our measurements over multi-orbit timescales (see Section 2.3). The fact that the overlapping light curve segments are so similar both in flux and in shape argues against a twice longer period, a possibility ground-based data left open (Radigan et al. 2012). The 2.39 hr and the 7.83 hr rotations are shorter than Jupiter's rotation period (~9.92 hr).

The left panel of Figure 2 displays the maximum and minimum spectra observed for both targets as well as their ratio (for clarity we do not plot the entire spectral series). The data are of superb quality (S/N > 300) and allow detailed analysis of the changes. Both targets show a strikingly similar pattern: only weakly wavelength-dependent broadband variations. For the precise shape of the variations, we refer the reader to the

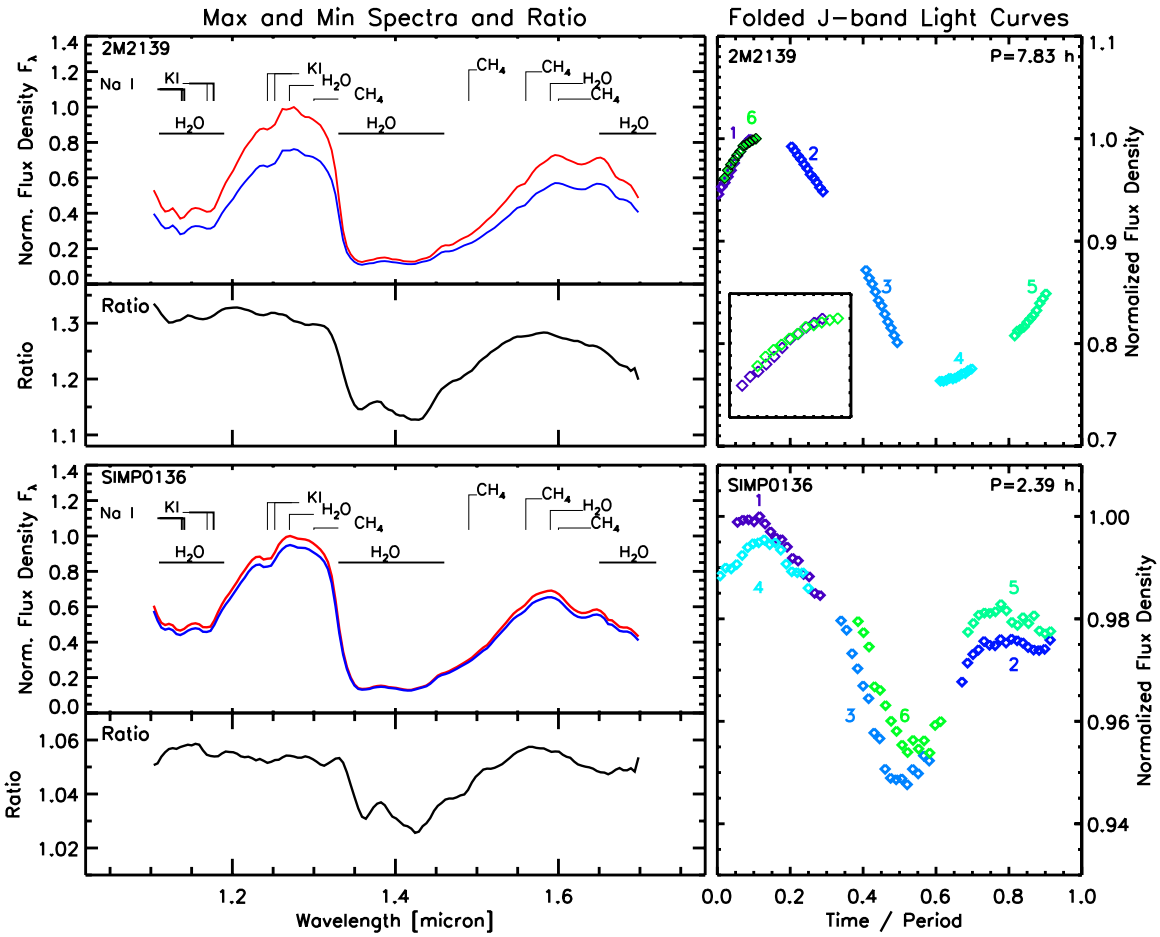

Figure 2. Spectra at the faintest and brightest stages of the two brown dwarfs show prominent water, potassium, and methane absorption features with similar depths. The ratio of the minimum over maximum spectra (minor panels on left) show variations with weak wavelength dependence in the continuum, and in the potassium, sodium, and methane features, but demonstrate lower-amplitude variations in the 1.4 μm water band. The period-folded J-band light curves (right) reveal variations in the surface brightness distributions of these two targets. Red and black colors show data from the first and sixth orbits for 2M2139, which perfectly overlap if a 0.5% flux scaling is allowed, consistent with the photometric stability on a 2σ level. In contrast, SIMP0136 displays light curve evolution over 5 hr present both in the absolute levels and the light curve shape at levels well above our uncertainties.

(A color version of this figure is available in the online journal.)

ratio panels in Figure 2 and here only highlight the peak of the ratios in the J and H bands. For 2M2139 the flux density change ΔF in the observed spectra peaks in the J band at 33% at 1.20 μm and in the H band at a level of 28% at 1.58 μm. For SIMP0136 ΔF peaks in the J band at 1.15 μm at 5.9% and $\Delta F_{1.56\,\mu\mathrm{m}}$ at a level of 5.8%. While the changes in the J and H bands are smooth and similar, in both sources the water absorption bands between ~1.32 and 1.50 μm vary at much lower levels: for example, $\Delta F_{1.4\,\mu\mathrm{m}} = 14\%$ for 2M2139 and $\Delta F_{1.4\,\mu\mathrm{m}} = 3.2\%$ for SIMP0136. Note that given our uncertainties of 0.25% for multi-orbit photometric stability (see Section 2.3) these differences are all highly significant. Surprisingly, with the exception of water all other gas-phase absorption bands (CH_4, Na I, and K I) change together with the continuum. The light curve of 2M2139 shows nearly sinusoidal variations, but SIMP0136 displays sharper, more structured variations.

3.1. Spectral Variations and PCA Analysis

Both light curves contain distinct and prominent higher-frequency components. We interpret these variations as spots with different spectra rotating in and out of the visible hemispheres of the targets. We use the detailed data sets to identify the spectra and spatial distribution of these spots and contrast this information with predictions of state-of-the-art atmosphere models.

We identify the smallest set of independent spectra, over the mean spectrum, that account for the majority of the observed variance by applying a principal component analysis (PCA). We computed the covariance matrix of the spectral time series over wavelengths of 1.1–1.7 μm, cutting off lower signal-to-noise regions outside this range. Eigenvectors ($\mathbf{E}_i$) and eigenvalues (Λ_i) of the covariance matrix were determined using the `LA_PACK` routine `LA_EIGENQL` in IDL. Components were sorted by eigenvalue, and the fractional contribution of each component to the overall variability is determined as $\Lambda_i/(\sum_i \Lambda_i)$, where the denominator is a sum over all eigenvalues.

Every observed spectrum at a given time, $\mathbf{S}(t)$, can then be approximated by a linear combination of the principal components,

$$\mathbf{S}(t) \approx \langle \mathbf{S} \rangle + c_0(t)\mathbf{E}_0 + c_1(t)\mathbf{E}_1 + \cdots, \quad (1)$$

where the series is truncated to include only components that contribute significantly above the noise level. The coefficients $c_i(t)$ are given by projections of the principal components onto the observed $\mathbf{S}(t) - \langle \mathbf{S} \rangle$.

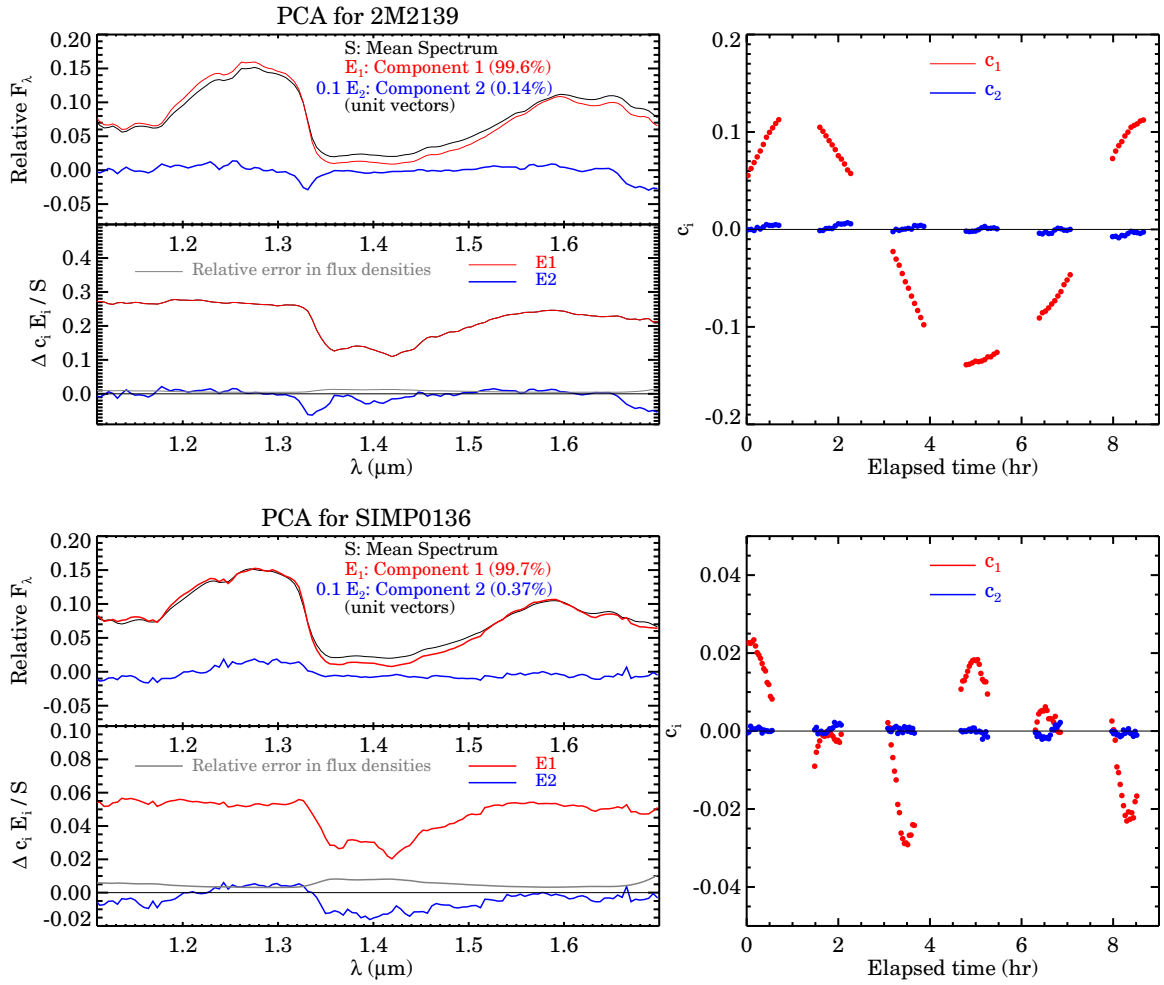

Figure 3. Principal component analysis of the time-series spectra for 2M2139 (top) and SIMP0136. Top left: the mean spectrum (black line) and first two principal components of the variability (red and blue lines, respectively). All components have been normalized as unit vectors. The contributions of each component to the total variability are indicated. Bottom left: the principal components plotted relative to the mean spectrum, multiplied by the maximum difference in their time projections, Δc_i. In other words, this panel shows the variability amplitude as a function of wavelength for isolated components. The relative error in flux densities is shown as a gray line for comparison. Right: projections of the principal components onto the data spectra as a function of time. The first component is dominant, producing a light curve that mirrors the broadband variations, while the second component appears to cycle with the *HST* orbits and may reflect low-level uncorrected systematic errors.
(A color version of this figure is available in the online journal.)

Perhaps surprisingly, variations of a *single* principal component account for 99.6% and 99.7% of the observed variability for 2M2139 and SIMP0136, respectively, with second components contributing at the 0.1% and 0.4% levels. In Figure 3, the mean spectrum and first two principal components ($\langle \mathbf{S} \rangle$, $\mathbf{E}_0$, and $\mathbf{E}_1$), as well as the time variability of the principal components ($c_i(t)$) are shown for both targets. In both cases, variations are given by $\mathbf{S}(t) \approx \langle \mathbf{S} \rangle + c_0(t)\mathbf{E}_0$, where only a single principal component is required to account for most of the observed variability. This implies that only *two* dominant spectra contribute to the observed variations (e.g., take $\mathbf{E}_0$ to represent the difference between two types of time-independent spectra $\mathbf{S}_2 - \mathbf{S}_1$), with the appearance of one "surface type" completely correlated with the disappearance of the other.

Thus, our major conclusion is that *only two types* of "surface" patches (e.g., cloudy and clear, or thick and thin clouds) are required to explain the observations in both of these sources. This finding validates a simple light curve model, applied below, in which the photosphere is describe by a linear combination of two 1D model atmospheres differing in cloud thickness and/or temperature.

3.2. Light Curve Analysis

Next we search for the simplest physically plausible surface brightness model that explains the observed light curve. We model the surface brightness distributions using the self-developed genetic algorithm-optimized mapping routine *Stratos* (described in the Appendix in detail). The only assumption of the model is that it describes surface features as elliptical spots with their major axes parallel to the rotational direction, an assumption that is motivated by the common outcome of simulations of hydrodynamical turbulent flows in shallow water approximation (e.g., Cho & Polvani 1996). (We note here that our two targets, just like all solar system giant planets, will be rotationally dominated with a Rossby number $R \ll 1$; Showman & Kaspi 2012). The input parameters of the model are the number of spots (i) and the number of different surface types allowed (2 in our case, as given by the PCA); the optimized parameters are the inclination and limb darkening of the brown dwarf, the surface brightness of each surface type, as well as five values for each spot (longitude, latitude, aspect ratio, area, and surface type). Possible solutions are ranked and optimized on the

basis of their fitness, which we define as the reduced chi-square difference between the observed and predicted light curves.

Interestingly, for both 2M2139 and SIMP0136 we find that models with *at least* three spots are required to explain the structured light curves: models with only one or two elliptical spots failed to reproduce the observed light curves. In Figure 8, we show the best-fit model, a non-unique, but representative solution for 2M2139. Additional models with somewhat different surface distributions are shown in Figure 9. Although the solutions are somewhat degenerate (as discussed in the Appendix) the best solutions for 2M2139 all agree in the following: (1) the overall longitudinal spot covering fraction distribution is similar (between 20% and 30%); (2) at least three spots are required; (3) the surface brightness of the spots typically differ by a factor of two to three (either brighter *or* fainter) from the surface, corresponding to approximately $\simeq$300 K difference in brightness temperature; and (4) the size of the largest spot extends about 60° in diameter. We note that more complex solutions with a higher number of spots are also possible, but these replace the larger spots with groups of smaller spots, without changing the general properties identified above.

An important property of all solutions is the presence of very extended spots or spot groups in the photosphere, which raises the question whether such large structures can exist in the fast-rotating, warm brown dwarfs. As for Jupiter, the gradient of the Coriolis force on our rotating targets is expected to break the atmospheric circulation into parallel jet systems (belts), which will limit the maximum size of continuous atmospheric structures. Here, we use the Rhines scale (e.g., Showman et al. 2011) to estimate the relative number of jet systems between our fast-rotating and slowly rotating sources: $N_{\rm jet} \simeq (2\Omega \times a/U)^{1/2}$, where Ω is the angular velocity, a is the brown dwarf radius, and U is the wind speed. If the maximum size of a feature (s_i) is limited by the jet width, the relative maximum spot sizes for two sources will be given by

$$\frac{s_1}{s_2} = \frac{\pi/N_{\rm jet,1}}{\pi/N_{\rm jet,2}} = \left(\frac{\Omega_1 a_1 U_2}{\Omega_2 a_2 U_1}\right)^{1/2}. \quad (2)$$

Further, for both sources a_1 and a_2 should closely approach 1 $R_{\rm Jup}$. If we assume that the wind speeds (U_1 and U_2) are similar in these two T2 dwarfs, the relative spot sizes in Equation (2) will be simply approximated by $s_1/s_2 = (P_2/P_1)^2$, arguing for $\sim$3.2$\times$ larger *maximum* spot surfaces on 2M2139 than on SIMP0136, in line with the larger amplitudes observed.

Based on the above considerations, we can also estimate the physical spot sizes. Although wind speeds are not known for brown dwarfs, in the following we explore the possible range. In estimating wind speeds only a few reference points are available: while the highest wind speeds ($U \simeq 2$ km s^{-1}) yet have been observed in the upper atmospheres of heavily irradiated hot Jupiters (e.g., Snellen et al. 2010), much lower wind speeds are typical for the cooler and only weakly irradiated atmospheres of solar system planets (typically 40–100 m s^{-1}, but up to $\simeq$300 m s^{-1} in Saturn). For a discussion on how brown dwarf circulation may fit in this picture we refer the reader to Showman & Kaspi (2012). We will now assume two bracketing cases: $U = 100$ m s^{-1} (Jupiter-like) and $U = 1000$ m s^{-1} (hot Jupiter-like). Our simple approximation with the low and high wind speeds would suggest $N_{\rm jet} \simeq 17$ and $N_{\rm jet} \simeq 5$, respectively, for the slowly rotating 2M2139 and $N_{\rm jet} \simeq 32$ and $N_{\rm jet} \simeq 10$, respectively, for the rapidly rotating SIMP0136. These values correspond to maximum latitudinal spot diameters of $\simeq$10° and $\simeq$36° for 2M2139, and $\simeq$6° and $\simeq$18° for SIMP0136. Thus, slower, Jupiter-like wind speeds would lead in small maximum features sizes (6°–10°), while high speeds would allow larger features (18°–36°). While we cannot accurately determine the wind speeds in our targets, the fact that these sources show large-amplitude variations emerging from large regions across their photospheres argues for wind speeds that are higher than those typical to Jupiter.

The simple predictions described above are consistent with the much larger variation seen in the slowly rotating 2M2139 than in its faster-rotating sibling and the predicted maximum spot sizes are similar to the size of the largest spots predicted by the best-fit light curve models of 2M2139 (Figure 2). With more data on varying brown dwarfs, a realistic treatment of the atmospheric circulation will be possible, replacing the simple argument introduced above.

3.3. Atmospheric Model Comparisons

Even the most capable state-of-the-art ultracool model atmospheres provide only imperfect fits to the fine structure of brown dwarf spectra; therefore, the full interpretation of our very high signal-to-noise spectral series is constrained by the fact that no existing model can accurately describe atmospheres at sub-percent accuracy. Nevertheless, the existing models can be used to explore the types of changes required to account for the observed color/magnitude variations. We proceed by identifying the best-fit atmosphere models for our two targets with the assumption that these models would well describe the dominant surface type on the targets. Then we explore what secondary surface types have to be added to account for the observed color–magnitude variations by adding a second model atmosphere.

We base our analysis on the state-of-the-art radiative–convective model atmospheres in and out of chemical equilibrium described in Burrows et al. (2006) and Madhusudhan et al. (2011), but also used an independent set of models by Allard et al. (2011) to verify that our conclusions are model-independent. The Burrows models include different empirical descriptions of the vertical structures of clouds of different condensates (Burrows et al. 2006). For each condensate, the vertical particle distribution is approximated by a combination of a flat cloud shape function and exponential falloffs at the high- and low-pressure ends. The cloud altitudes are defined by the intersects of the temperature–pressure profile and the condensation curves. The tested models included cloud shape functions with constant vertical distribution of particles above the cloud base (B-clouds, qualitatively consistent with the DUSTY models described in Allard et al. 2001), and different parameterizations of the generic cloud shape function (A, C, D, E in Burrows et al. 2006). Of particular interest is cloud type E, a generic cloud with very steep exponential falloffs corresponding to thin clouds thought to be typical to clouds composed of a single refractory condensate's large grains.

The spectra we explored ranged in temperature from 600 K to 1800 K with steps of 100 K, included solar and 10$\times$ sub-solar metallicities, and log $g = 4.0$ and 5.0 for the Burrows et al. (2006) models and log $g = 4.0$, 4.5, and 5.0 for the Allard et al. (2001) models. Figure 4 shows our two targets and the best-fit spectra and templates. The upper models are from the BT-SETTL series from Allard et al. (2011), which we plot for comparison, while the lower curves are model calculations based on models described in Madhusudhan et al. (2011). The field brown dwarf spectral templates are from Leggett et al.

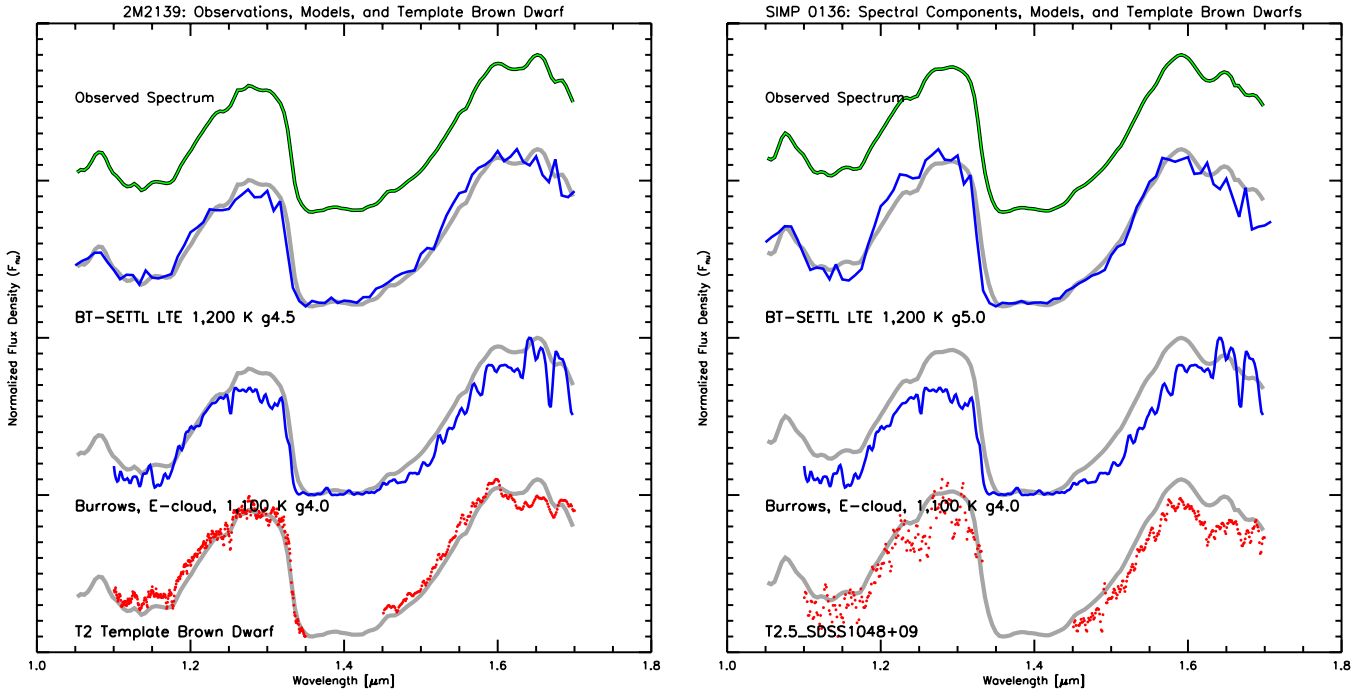

Figure 4. Comparison of the observed peak spectra (green), normalized theoretical model atmospheres (blue), and field brown dwarf spectral templates (red). The top model curves are from Allard et al. (2011), while the lower models are based on Burrows et al. (2006).
(A color version of this figure is available in the online journal.)

(2000) and Chiu et al. (2006). We find that for 2M2139 the best-matching spectral template is a T2-type template, while for SIMP0136 a T2.5 provides a good match.

Both sources can be fit well with a BT-SETTL model in local thermodynamical equilibrium and an effective temperature of 1200 K, but fitting the spectrum of 2M2139 requires a lower surface gravity ($\log g = 4.5$) than SIMP0136, which is better matched by a higher surface gravity model ($\log g = 5.0$). Fits with the Burrows models suggest slightly lower temperatures. Given the coarser spacing of the surface gravity grid of the Burrows models we used $\log g = 4.0$ for 2M2139 and $\log g = 5.0$ for SIMP0136. Although the lower surface gravity fits better our spectra, due to its limited wavelength coverage we take these $\log g$ values as comparative but do not argue that they represent accurate characterization of the surface gravity (see also, e.g., Cushing et al. 2008 for the difficulty of determining precise atmospheric parameters from single-band spectroscopy). The modal grain sizes are an adjustable parameter in the Burrows models and models with large grains provided the best match for 2M2139. We note that this model comparison is based on *peak-to-valley normalized* spectra, i.e., it focuses on the spectral shape rather than the absolute J, H brightnesses—we do so because our sources show strong J-, H-band variations and only weak variations in the spectral shape.

After establishing the best-fit starting model for the two sources, we explore what secondary surface type is required to explain the observed color–magnitude variations. Our tool for this step is the near-infrared color–magnitude diagram (CMD) shown in Figure 5. Here, we plotted a full sequence of L/T dwarfs using the parallax and near-infrared photometric database by Dupuy & Liu (2012). Fully cloudy L-type brown dwarfs typically appear bright and red, while the dust-free atmospheres of T-type brown dwarfs are blue and faint. Transition objects are seen to show brighter J-band magnitudes with later spectral types before an eventual turn to the clear T-dwarf sequence (Dahn et al. 2002; Tinney et al. 2003; Vrba et al. 2004).

Next, we tried to vary each model parameter separately to assess its effect with the observed variations. We found that *no* combination of models with a difference only in a single parameter (temperature, cloud scale height, and the presence or the absence of cloud layer) can introduce the observed changes (see dashed black lines lower right panel in Figure 5): the tracks along which the source would vary on the CMD if such a secondary surface type would be added is clearly inconsistent with the actual variations. The same conclusion was reached by Artigau et al. (2009) for SIMP0136 based on comparison of models by Allard et al. (2003) and Tsuji (2005) to their ground-based $\Delta J/\Delta K$ observations and by Radigan et al. (2012) for 2M2139 through comparison to models by Saumon & Marley (2008).

We next explored *correlated* changes in parameter pairs. We found that correlated changes in cloud scale height and temperature are required (green dashed lines in Figure 5). By allowing these two model parameters to vary together we find that thin clouds in combination with large patches of cold and thick clouds (i.e., $T_{\rm eff} = 1100$ K models with E-type clouds and 800 K B-type clouds, green dashed lines) can explain well the observed color–magnitude variations (blue and red crosses).

This solution requires about 300 K temperature difference between the spots and the surface, fully consistent with the factor of three surface brightness change predicted by our light curve shape model. Our models also predict the relative surface covering fraction for the thin and thick clouds (given as percentages in Figure 5), which are also consistent with the surface model shown in Figure 8.

We note that qualitatively similar results were obtained for 2M2139 using a ground-based photometric data set and models of Saumon & Marley (2008) by Radigan et al. (2012).

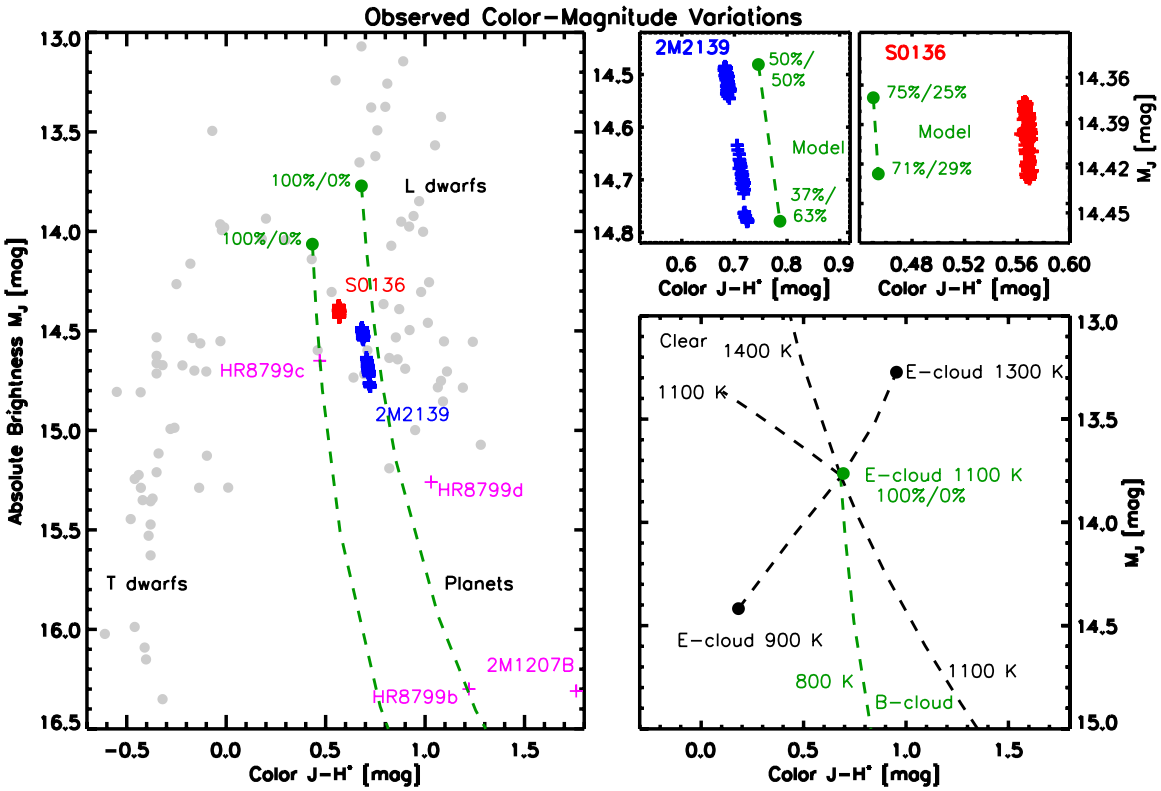

Figure 5. Near-infrared color–magnitude variations of our targets (blue and red) in the context of warmer cloudy L-dwarfs and cooler cloud-free T-dwarfs (in gray from Dupuy & Liu 2012). Brightness variations in 2M2139 and SIMP0136 occur without strong color changes (top right and middle right panels). Lower right: changes predicted by varying single model parameters (black dashed lines) are inconsistent with the observations. The green dashed lines show that simultaneously changing cloud structure (thin to thick) and temperature provides a perfect match. The direction of the modeled changes in 2M2139 and SIMP0136 (green dashed line) is compatible with the poorly understood underluminosity of several directly imaged giant planets (shown in magenta). The percentages show the covering fraction of thin and thick clouds, respectively.

(A color version of this figure is available in the online journal.)

4. DISCUSSION

4.1. A Single Spot Type

Because of the richness of possible condensates in brown dwarf atmospheres one may expect a complex mix of cloud properties, composition, and cloud scale height to be represented even within a single brown dwarf atmosphere. The observational fingerprint of such surface complexity in a rotating brown dwarf would be multi-component, complex changes in the spectra, brightness, and color. In stark contrast, the two sources observed show a single distinct type of simple change. This is reflected, for example, in the single-direction track in the CMD (Figure 5). The PCA analysis (see Section 3.1) reveals that all the observed variance in the two sources can be reproduced with the combination of *only two* different spectra. This surprising result shows that all major features in the visible photosphere, although distributed across both hemispheres of each target, share the same spectra (i.e., same deviation from the mean spectrum).

We note that based on spectral fits from composite near-infrared spectra Burgasser et al. (2010) has identified 2M2139 as a strong candidate for being an unresolved binary brown dwarf. These authors argue that 2M2139 could be matched better, although imperfectly, by a blend of an L7–L9.5 and a T3.5–T4.0 binary than by any single template brown dwarf. It is tempting to consider the possibility that the fit by two blended spectra in this case is not the sign of an unresolved binary, but instead emerges from the blend of two different surface types on the source (as also proposed by Khandrika et al. 2013; Radigan et al. 2012)—one with a spectrum of an L8.5 ± 0.7 dwarf, the other with a spectrum of a T3.5 ± 1.0 dwarf. However, this explanation is unlikely to be correct. A composite spectrum of two such dwarfs with time-varying weights due to the rotation would introduce J versus $J–H$ color variations in the direction of the L–T transition, very different from what we observed (see Figure 5).

The fact that flux density in the observed molecular bands—with the exception of the less-changing water band—varies together and at the same rate as the continuum shows that the opacity variations in the targets *cannot* originate from changes in the abundances of the common gas-phase absorbers, such as methane. Based on comparison to atmosphere models we argue that these spots are patches of very thick clouds. The fact that any two such cloud patches would share the same spectra, different from the dominant spectrum of the sources, argues for the presence of a *single mechanism* to form these thick cloud patches. Possibilities, as explored below, include circulation and large-scale vertical mixing.

4.2. Complex Surfaces

With our surface mapping tools (see Section 3.2) we find that both sources have relatively complex surface brightness distributions: assuming elliptical spots, no one- or two-spot model can reproduce the structure of the light curves. While our model is not able to deduce the precise appearance of the

photosphere, it provides useful insights into the complexity and overall distribution of the thick cloud patches observed. Specifically, the light curve and our models reveal that a large fraction of the surface of both targets is covered by the cloud patches. These patches may be very large single structures (corresponding to our simplest model) or they may be super-structures, consisting of dozens or even hundreds of smaller cloud patches with the same surface covering fractions. Whether single or complex structures, however, any mechanism that explains the spectral appearance and high cloud scale height, needs to account for the concentration of these patches on the surface of the targeted brown dwarfs.

We note here that the light curve modeling is only sensitive to the varying surface components, because homogeneously distributed features will not introduce brightness variations. Thus, it is likely that the large patches deduced from the light curve are not the only features present in the photosphere. Reinforcing this possibility is the fact that color–magnitude modeling based on model atmospheres (Section 3.3) suggests similar level of asymmetry but on top of a more symmetric component. According to the best-fit model atmosphere combination, the fraction of surface covered by thick clouds varies from about 50%–63% on the visible 2M2139, while it occupies only 25%–29% of the surface of SIMP0136 (see Figure 5). Thus, the modeling suggests that most of 2M2139's surface is covered by thick clouds with large thin patches (that are brighter and contribute most of the observed emission), while SIMP0136 has an overall thin cloud layer with large patches of thick clouds. Although the covering fractions are different, based on the overall similarity of the spectra and the spectral variations these two sources have very similar thin and thick cloud layers.

The complex distribution of otherwise similar or identical thick cloud patches also offers opportunity for further exploration of the dynamics of brown dwarf atmospheres. Cloud structures are subject to multiple dynamical processes and are likely to evolve on a broad range of timescales. For example, the structure of the light curves may evolve due to differential rotation, an effect that should be observable with high-precision data set covering sufficient baselines. Other processes, such as thick cloud formation (i.e., rapid increase of the cloud scale height) or the reverse of this process, rain out of the condensate grains, may also result in changes over relatively short timescales.

4.3. Thin and Thick Clouds, but No Deep Holes

A leading hypothesis to explain the dramatic spectral changes observed to occur at the L/T transition invokes a breaking apart of the cloud cover (e.g., Ackerman & Marley 2001; Burgasser et al. 2002). This idea provided motivation for our initial observations, and predicts surfaces consisting of clouds and holes that act as windows into the deeper photosphere. The most simple picture, and the one that has been explored by models (Burgasser et al. 2002; Marley et al. 2010), is one where holes in the cloud layer represent pure clearings, 100% free of condensate opacity. In contrast to this assumption, our observations of two of the most variable brown dwarfs suggest that dark and bright regions of the photosphere represent thick and thin cloud regions rather than cloudy and cloud-free regions (Section 3.3). This may reflect holes in a thick cloud layer that look down into a thinner cloud layer. More generally, our observations argue for a more complex picture of cloud heterogeneities than envisioned with simple cloudy and cloud-free models. A similar conclusion was arrived at by Radigan et al. (2012), who found that *JHK* photometric

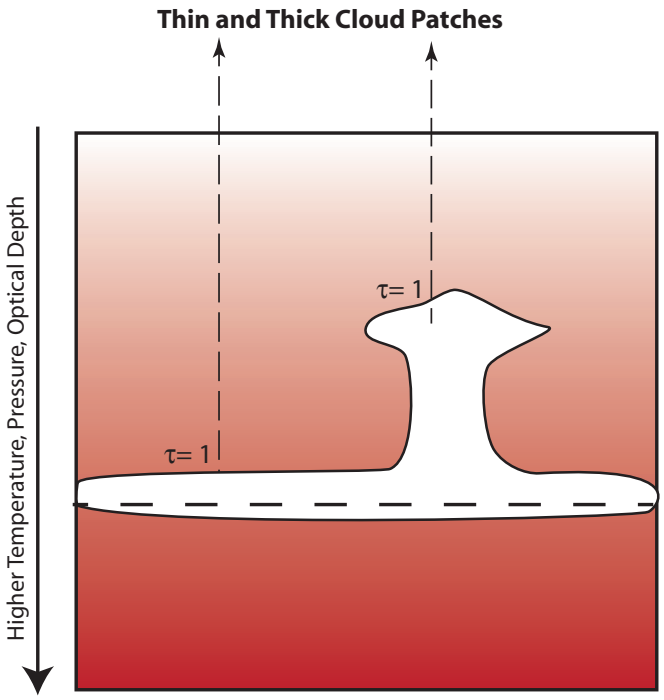

Figure 6. Sketch illustrating a possible cloud structure consistent with the observations, which argue for large-scale variations in dust cloud scale height, correlated with a change in temperature. Higher clouds will limit the observed column to the cooler upper atmospheres, explaining the correlated changes in temperature and cloud scale height. More complex configurations, such as multi-layer clouds, are also possible.

(A color version of this figure is available in the online journal.)

monitoring of 2M2139 was inconsistent with the presence of cloud-free regions, based on models of Saumon & Marley (2008). Thus, both photometric observations out to the *K* band and spectroscopic observations from 1 to 1.7 μm argue against the existence of cloud-free regions.

We also found that the cloud thickness variations are correlated with changes in the effective temperature of the secondary model. This correlation is not surprising: the higher the dust scale height, the shallower the pressures and the lower the temperatures visible to the external observer (see Figure 6). This correlation, thus, argues for patches of thick clouds towering over the otherwise thinner cloud layer covering most of the hemispheres of the targets.

The vertical structure and composition of these thick clouds is an exciting question, albeit one our current data do not constrain well. Recently, Buenzli et al. (2012) have shown that by combining data over a broad wavelength range—where different wavelengths probe different atmospheric depths—the vertical structures of the clouds can be explored. In their study five atmospheric layers of a T6.5 dwarf's were sampled by obtaining five complete light curves at depths ranging from 0.1 to ~10 bar. An important and surprising result of their study was a significant and pressure-dependent phase difference in the atmosphere with the largest phase shift observed at the deepest level exceeding 180°. While a full analysis like that carried out by Buenzli et al. (2012) is beyond the scope of this paper, we show in Figure 7 that the same narrowband light curves as used by those authors, when extracted from our spectral series, show no significant phase shift. Thus, while the results of the T6.5 brown dwarf suggest correlated large-scale vertical–horizontal

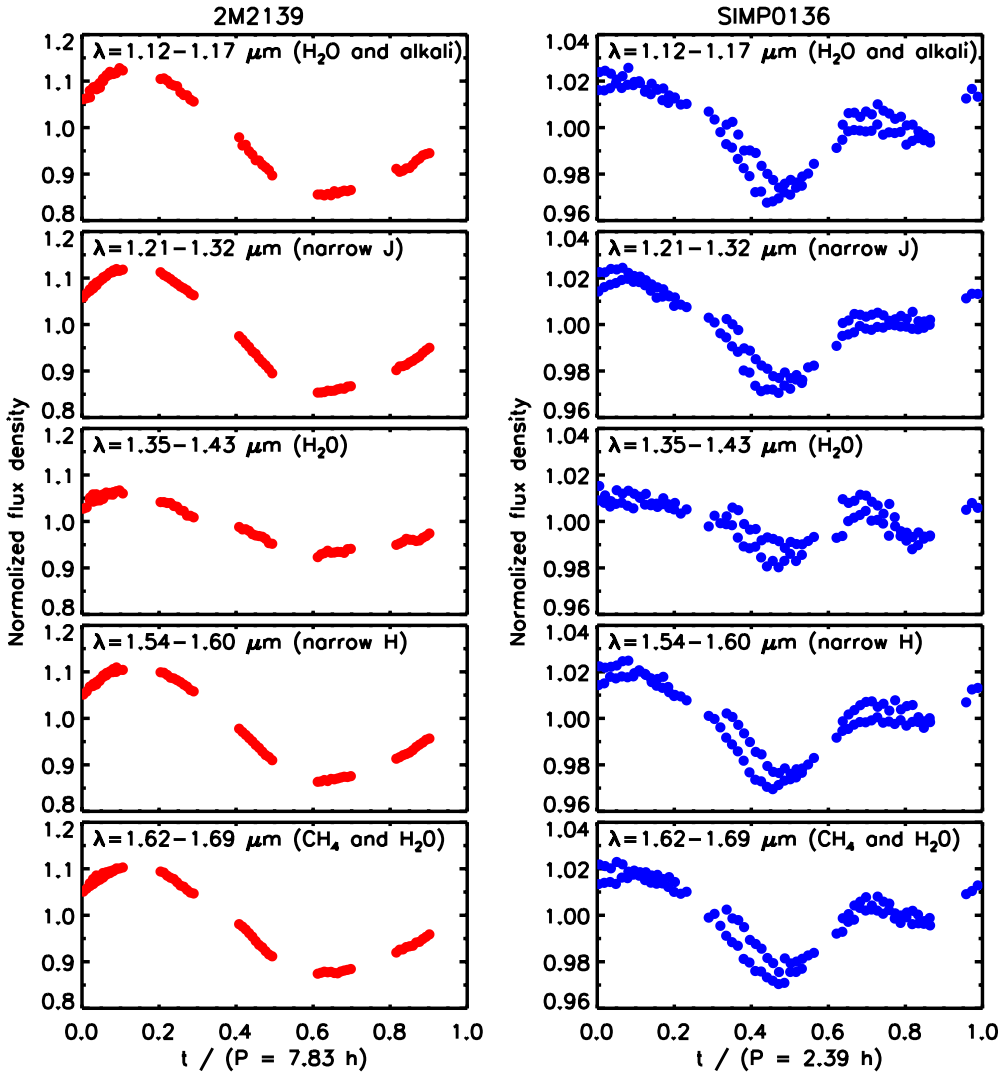

Figure 7. Five narrowband light curves extracted from the spectral series for the two targets show that the light curve changes are all occurring at the same phase. The spectral bands have been selected to probe specific atmospheric depth and match those adopted by Buenzli et al. (2012). In contrast to the no phase shift seen in our two T2 dwarfs, the T6.5 dwarf analyzed by Buenzli et al. (2012) showed a very prominent pressure-dependent phase shift in the same narrowband light curves, revealing a large-scale horizontal–vertical structure.

(A color version of this figure is available in the online journal.)

structures, the two early-T dwarfs studied here show similar cloud structures at different layers without phase differences.

4.4. Apparent Underluminosity due to Thick Clouds

The remarkable cloud scale height variations in our targets demonstrate how this parameter affects the brightness of ultracool atmospheres. Thick clouds persisting at temperatures lower than typical for brown dwarfs have been proposed as one of the processes that may explain the apparent underluminosity of directly imaged giant exoplanets compared to brown dwarfs with similar spectral morphology (magenta crosses in Figure 5; see also Skemer et al. 2012; Barman et al. 2011a, 2011b; Currie et al. 2011; Madhusudhan et al. 2011; Marley et al. 2012). Several authors propose that such unusually thick clouds would be present in directly imaged exoplanets due to the low surface gravities of these sources, which provides an attractive and self-consistent explanation for the appearance and low occurrence rate of these sources. However, the effects of thick clouds remained difficult to verify, as multiple parameters (metallicity, surface gravity, age, mass, chemistry, and cloud structure) vary simultaneously between any two ultracool atmosphere. The novelty of our observations is that they are comparing *different cloud structures* within the *same atmospheres*, i.e., keeping metallicity, surface gravity, age, mass, and bulk composition constant. This allows the effects of cloud structure to be isolated. We note that a minor caveat here is that the pressure–temperature profile of atmospheres with large spots may differ from those with only thick *or* thin clouds; thus, the thick clouds' impact must be evaluated keeping this possible difference in mind.

We can explore the effect the thick clouds would have by extending their surface covering fraction in our model beyond that observed in our targets, i.e., by increasing the surface covering fractions of the thick cloud patches to values approaching 100%. The resulting green dashed line in Figure 5 shows that increasing thick cloud coverage will produce color–magnitude tracks crossing the positions of the directly imaged planets (magenta crosses). Thus, if the thick cloud patches we observed in the atmospheres of our T2 targets would cover their complete or near-complete atmospheres, their near-infrared brightness and colors would provide a good match to the directly imaged

exoplanets. These results lend support to the models in which the peculiar color and brightness of exoplanets is introduced by thick clouds, but we note that in this work no attempt was made to match the spectra predicted by our simple models to those observed by exoplanets. While our observations cannot identify the cause for the thick clouds in exoplanets, we expect that any successful model for the thick clouds in faint and red exoplanet atmospheres will also provide an explanation for the coexistence of thin and thick clouds in L/T transition brown dwarfs.

4.5. The Path to Next Generation Atmosphere Models

Our observations provide exceptionally high signal-to-noise spectra that probe spectral variations within the photospheres of brown dwarfs. The accuracy of this data set is high enough that finding a perfect match (<1%) with existing atmosphere models was not possible, demonstrating the limitations of the existing models. Although the best-fit spectra match the mean spectrum to typically within 5%–10% in the spectral range studied, which are typically considered to be good fits for brown dwarf atmospheres, these differences are comparable to or larger than the amplitude of changes we observe in our spectral series. Therefore, the accuracy of the existing models used in this paper did not allow meaningful modeling of the entire spectral series yet. Instead, in our modeling procedure we started from atmosphere models that provided best fits to the mean spectra of the targets and then explored their *color variations*. Our approach to model a patchy cloud cover with a linear combination of independent 1D models is imperfect and it is likely not physically self-consistent due to the somewhat different pressure–temperature profiles of these models (e.g., Marley et al. 2010, 2012).

It is worthwhile to briefly explore the limitations of current models and potential pathways to improve them. Arguably, the key limitations are the incomplete molecular opacity databases and the fundamentally 1D nature of most atmosphere models. Expanding and refining the opacity databases relies on the continuation of ongoing laboratory and theoretical efforts and not limited by the observations of ultracool atmospheres. In contrast, constraining and further developing two- or three-dimensional models (e.g., Freytag et al. 2010) will require more accurate data sets and, in particular, data sets that provide spectrally and spatially resolved information. We anticipate that the brown dwarf spectral mapping technique introduced in this paper will lead to a major step in testing and refining physically realistic models of cloud formation and cloud structure (e.g., Helling et al. 2008a, 2008b) and atmospheric dynamics (Freytag et al. 2010; Showman & Kaspi 2012)

4.6. Spectral Mapping of Ultracool Atmospheres

In this paper we also applied a method, spectral mapping, to a new class of objects, ultracool atmospheres. As a new method for this field we now briefly discuss its potential and future uses. Photometric phase mapping has been proposed early on to reach spatial information beyond the diffraction limit (e.g., Russell 1906). Since then, different variants of this idea have been used successfully to derive asteroid shapes from photometry (e.g., Kaasalainen et al. 2001; Kaasalainen & Viikinkoski 2012), to map their surface composition from spectral mapping (e.g., Binzel et al. 1995), to map starspots via photometry and Doppler imaging (e.g., Budding 1977; Vogt et al. 1987; Lüftinger et al. 2010), and to translate precision *Spitzer* photometry to one-dimensional and two-dimensional brightness distributions for hot Jupiters (e.g., Knutson et al. 2007; Cowan et al. 2012; Majeau et al. 2012). Similarly to the hot Jupiter studies, in an upcoming study, Heinze et al. (2013) use precision *Spitzer* photometry complemented by ground-based near-infrared light curve to explore cloud properties on an early L-dwarf. Most recently, Buenzli et al. (2012) have found pressure-dependent phase shifts in multi-band light curves extracted from the *HST* spectral series and a *Spitzer* 4.5 μm light curve of a T6.5 brown dwarf, revealing vertical structure in an ultracool atmosphere for the first time.

The method used here is a logical next step in these brown dwarf studies, where a large time-resolved spectral set is used to identify the diversity, spatial distribution, and spectra of the key photospheric features. Further similar studies with space-based instruments on *HST* and *Spitzer*, complemented by sensitive ground-based photometric observations, will allow obtaining data similar to those presented here on brown dwarfs covering a much broader range of atmospheric parameters. Such a data set will allow the exploration of the properties of cloud cover with spectral type, surface gravity, and rotation period, an important step toward establishing a physically consistent picture of condensate clouds. Next-generation adaptive optics systems will also be capable of measuring relatively small photometric variations in directly imaged giant exoplanets, allowing comparative studies of brown dwarfs and extrasolar giant planets (Kostov & Apai 2012).

The changes observed in SIMP0136, first reported in Artigau et al. (2009) and also seen in our Figure 2, also highlight another exciting question. Cloud covers in some brown dwarfs clearly change on very short timescales on very significant levels, offering an opportunity to study the atmospheric dynamics of ultracool atmospheres via multi-epoch, multi-timescale, and multi-wavelength observations.

Spectral mapping is set to be a powerful new method not only to characterize brown dwarf atmospheres, but also extrasolar planets.

5. SUMMARY

In summary, we apply spectral mapping for the first time on ultracool atmospheres and show that two L/T transition brown dwarfs have patchy cloud covers with multiple (>3) large spots/structures. Analysis of the spectral variations shows that a linear combination of only two types of spectra can explain the variance observed in both sources, demonstrating the presence of a single type of photospheric feature in an otherwise homogeneous cloud cover. We find that light curves derived from narrow wavelength sections of the spectra all change in phase. The observed variations show that the near-infrared brightness of dusty brown dwarfs can decrease significantly (3%–27%) with only a modest reddening in the $J-H$ color. These changes and extrapolation from the atmospheric models fitting them closely resemble the properties of red and "underluminous" directly imaged exoplanets, arguing for thick clouds causing the underluminosity of giant planets. Our models with large cloud thickness variations and correlated temperature variations ($\simeq$300 K) explain the observed light curves (amplitudes and color–magnitude changes) as well as the light curve structures. Our findings reinforce models that explain the underluminosity of directly imaged super-Jupiters with large-scale height dusty atmospheres.

The technique applied here, rotational phase mapping, provides a powerful tool to study the atmospheres of ultracool objects, brown dwarfs, and exoplanets. Cooler objects may

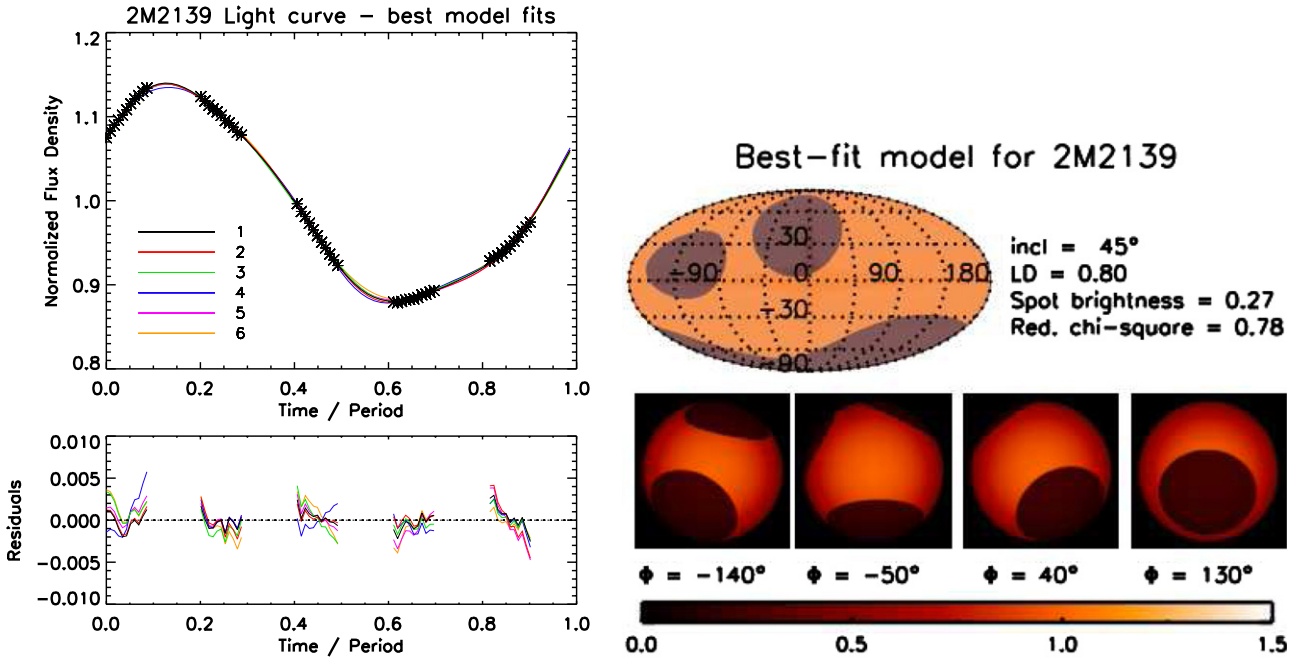

Figure 8. Left: the *Stratos* package provides multiple, broadly similar models that can reproduce well the observed light curve of 2M2139. All models require at least three distinct spots. Models are numbered by increasing chi-square and shown in Figure 9. Right: example best-fit model for 2M2139. Although some parameters are degenerate, all models require multiple large spots distributed across the surface of the source in a broadly similar pattern.

(A color version of this figure is available in the online journal.)

harbor clouds of particles with various composition (NH_3, CH_4, and H_2O) and phase (solid or liquid), the presence of which can be inferred with this technique. Its full potential, however, can be achieved with a telescope like *James Webb Space Telescope*, which will couple high sensitivity and broad wavelength coverage with high contrast, enabling spectrally and spatially resolved mapping of directly imaged exoplanets.

We acknowledge the anonymous referee, whose comments improved the manuscript. Support for Program number GO-12314 was provided by NASA through a grant from the Space Telescope Science Institute, which is operated by the Association of Universities for Research in Astronomy, Incorporated, under NASA contract NAS5-26555. The work of J.R. and R.J. was supported by grants from the Natural Sciences and Engineering Research Council of Canada.

We are grateful to the dedicated staff at the Space Telescope Science Institute for their outstanding support of the observations and the instrumentation.

Calibrated data and reference files used in this work are available indefinitely at the B. A. Mikulski Archive for Space Telescopes (http://archive.stsci.edu). We acknowledge an STScI Directors Discretionary Grant that helped the start of this project.

Facility: HST (WFC3)

APPENDIX

SURFACE MAPPING: THE STRATOS PACKAGE

Translating a light curve into the surface map of a rotating sphere is an underconstrained deconvolution problem. Although due to the nature of the problem not all information can be retrieved, equipped with a few priors about the physically plausible geometries and a very high signal-to-noise data it is possible to derive meaningful maps with robust characteristics.

To model our data we developed a new IDL package (*Stratos*). In the following, we briefly describe the principles and organization of this package and then discuss the solutions and degeneracies in the derived parameters. In *Stratos*, we apply an optimized forward-modeling procedure to identify the best-fitting two-dimensional map for each spectral series given a small set of a priori assumptions.

We start by using PCA to identify i, the number of independent spectral components required to explain at least 96% of the observed spectral variance (see Section 3.1 for both of our sources $i = 2$). This determines the number of types of surface features we include in our model, including the ambient spectrum. Our actual surface model consists of a sphere with j ellipses in its photosphere. The surface brightness level of each of these ellipses is fixed to one of the i distinct levels. Thus, the basic free parameters of the model are the latitude, longitude, axes ratio, and area of each ellipse, i.e., four parameters per ellipse. The relative brightness of the i different surface types are also free parameters (in our case only a single parameter). In addition to these parameters we add the inclination of the targets spin axis and the limb darkening as free parameters. We express limb darkening in the commonly used form as $I(\phi) = I_0 \times (1 - c \times (1 - \cos(\phi))$, where ϕ is the angle between the line of sight and the observed surface element and c is the limb-darkening coefficient fitted. We allowed c to vary between 0 and 0.8, the former representing no limb darkening and the latter upper bound corresponding to the strongest limb darkening predicted in near-infrared wavelengths for low-mass stars (Claret & Bloemen 2011).

We optimize the above model using a genetic algorithm, a commonly applied heuristic optimization algorithm (see, e.g., Charbonneau 1995). We define the fitness of each solution by the sum of the squared differences between the predicted and

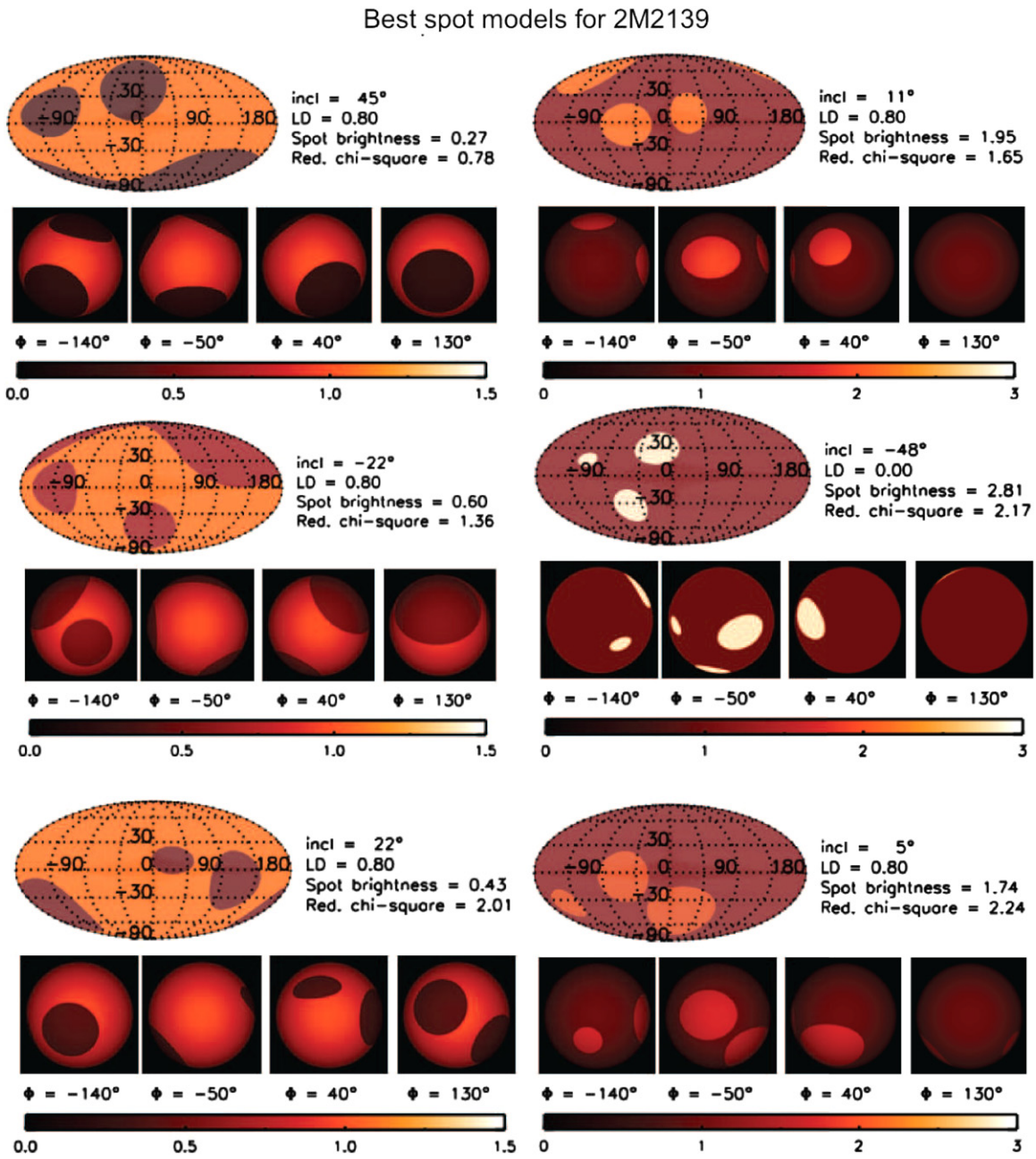

Figure 9. Although light curve decomposition yields degenerate solutions, several key properties of the solutions are similar. No solution with less than three spots can fit the data; the relative spot sizes and total covering fractions of the models are very similar. When the inclinations are considered, the spot distributions are also similar. While no unique solution exists, the modeling provides an insight into the similarities of the simplest best-fitting models.

(A color version of this figure is available in the online journal.)

observed spectral variations. Multiple parallel optimization runs were executed on a 12-core Intel Xeon-based Mac Pro; typical runtimes are about two days per target.

The maps derived with phase mapping and *Stratos* have three natural limitations. First, our data are sensitive to variations in the surface brightness distributions and insensitive to time-invariant features. Second, the observations can only probe the visible fraction of the photosphere: for a rotation axis inclined with respect to the plane of the sky part of the photosphere will not be visible at any rotation phase. Third, a variation in the latitude of any feature only slightly changes the light curve.

The above limitations lead to solutions that are degenerate in some parameters, while robust in others. In the following, we discuss the similarities and degeneracies in the best-fit solutions.

During a typical fitting procedure *Stratos* evaluates about $\simeq 10^5$ different solutions. Figure 9 shows the light curves for the six best-fit models for 2M2139, the target with the highest signal-to-noise levels. Note that the light curves predicted by the six models differ the most in the inter-orbit gaps, where *HST* could not obtain data. These models provide excellent fits and the amplitude of the residuals are less than 0.5% (Figure 8).

Figure 9 provides an overview of the six best-fit surface maps. From first glance these solutions may appear different, but even cursory inspection reveals that all solutions share several key characteristics. First, three spots provide excellent fits to the observations, whereas no one- or two-spot solution was acceptable. Second, the longitudinal distributions of the visible surface area occupied by lighter and darker features are very

similar. Third, the projected sizes and relative positions of the two larger spots are also similar when considering the inclination of the model. Clearly, there are also several parameter pairs that are degenerate and not tightly constrained: the inclination and the limb darkening and, to a lesser degree, the spot size and the spot surface brightness.

Bright spot/dark spot degeneracy. Our surface modeling procedure can model the light curves equally well with large bright spots on darker surface or with large darker spots on a lighter surface. These solutions—when the inclination and the latitudinal integration is considered—appear to be inverses of each other and, ultimately, lead to the same longitudinal 1D surface brightness distribution. At the level of accuracy of our measurements these two families of solutions are degenerate, although they may be distinguishable in the future with more precise data sets and a shape model for the features. In the context of our atmospheric modeling the darker regions can be interpreted as covered by thick clouds, while the brighter regions are covered by thinner clouds with a higher-pressure upper boundary (i.e., warmer). Whether the photosphere should be interpreted as a thin cloud layer with towering thick clouds or a thick cloud layer with depressions or cavities (but not deep holes) depends on the covering fraction of the two surface types. The atmospheric modeling (see Section 3.3 and Figure 5) provides guidance on the probable relative covering fractions: the models suggest a thin cloud cover varying between 71% and 75% for SIMP0136 (i.e., dominantly darker spots in a lighter photosphere) and between 37% and 50% thin cloud cover for 2M2139. However, this comparison is imperfect: our light curves are sensitive to changes in the surface covering fractions and insensitive to azimuthally symmetrically distributed photospheric features. Such features—bands or evenly distributed small spots—would not influence the light curves (i.e., distribution of the darker/lighter surface features), but would influence the relative photospheric covering fraction of the atmospheric models used. We foresee that our data set and similar data sets will be modeled in the near future by *simultaneously* fitting the mean spectra, the spectral changes, and the light curve shapes in a self-consistent manner, instead of the three-step procedure we followed here.

REFERENCES

Ackerman, A. S., & Marley, M. S. 2001, ApJ, 556, 872
Allard, F., Guillot, T., Ludwig, H.-G., et al. 2003, in IAU Symp. 211, Brown Dwarfs, ed. E. Martín (San Francisco, CA: ASP), 325
Allard, F., Hauschildt, P. H., Alexander, D. R., Tamanai, A., & Schweitzer, A. 2001, ApJ, 556, 357
Allard, F., Homeier, D., & Freytag, B. 2011, in ASP Conf. Ser. 448, 16th Cambridge Workshop on Cool Stars, Stellar Systems, and the Sun, ed. C. Johns-Krull, M. K. Browning, & A. A. West (San Francisco, CA: ASP), 91
Allers, K. N., Kessler-Silacci, J. E., Cieza, L. A., & Jaffe, D. T. 2006, ApJ, 644, 364
Artigau, É., Bouchard, S., Doyon, R., & Lafrenière, D. 2009, ApJ, 701, 1534
Barman, T. S., Macintosh, B., Konopacky, Q. M., & Marois, C. 2011a, ApJ, 733, 65
Barman, T. S., Macintosh, B., Konopacky, Q. M., & Marois, C. 2011b, ApJL, 735, L39
Binzel, R. P., Bus, S. J., Xu, S., et al. 1995, Icar, 117, 443
Budding, E. 1977, Ap&SS, 48, 207
Buenzli, E., Apai, D., Morley, C. V., et al. 2012, ApJL, 760, L31
Burgasser, A. J., Cruz, K. L., Cushing, M., et al. 2010, ApJ, 710, 1142
Burgasser, A. J., Geballe, T. R., Leggett, S. K., Kirkpatrick, J. D., & Golimowski, D. A. 2006, ApJ, 637, 1067
Burgasser, A. J., Looper, D. L., Kirkpatrick, J. D., Cruz, K. L., & Swift, B. J. 2008, ApJ, 674, 451
Burgasser, A. J., Marley, M. S., Ackerman, A. S., et al. 2002, ApJL, 571, L151
Burningham, B., Leggett, S. K., Homeier, D., et al. 2011, MNRAS, 414, 3590
Burrows, A., Hubbard, W. B., Lunine, J. I., & Liebert, J. 2001, RvMP, 73, 719
Burrows, A., Sudarsky, D., & Hubeny, I. 2006, ApJ, 640, 1063
Charbonneau, P. 1995, ApJS, 101, 309
Chauvin, G., Lagrange, A.-M., Dumas, C., et al. 2005, A&A, 438, L25
Chiu, K., Fan, X., Leggett, S. K., et al. 2006, AJ, 131, 2722
Cho, J. Y.-K., & Polvani, L. M. 1996, PhFl, 8, 1531
Claret, A., & Bloemen, S. 2011, A&A, 529, A75
Cowan, N. B., Machalek, P., Croll, B., et al. 2012, ApJ, 747, 82
Cruz, K. L., Reid, I. N., Kirkpatrick, J. D., et al. 2007, AJ, 133, 439
Currie, T., Burrows, A., Itoh, Y., et al. 2011, ApJ, 729, 128
Cushing, M. C., Marley, M. S., Saumon, D., et al. 2008, ApJ, 678, 1372
Cushing, M. C., Saumon, D., & Marley, M. S. 2010, AJ, 140, 1428
Dahn, C. C., Harris, H. C., Vrba, F. J., et al. 2002, AJ, 124, 1170
Dupuy, T. J., & Liu, M. C. 2012, ApJS, 201, 19
Folkes, S. L., Pinfield, D. J., Kendall, T. R., & Jones, H. R. A. 2007, MNRAS, 378, 901
Freytag, B., Allard, F., Ludwig, H.-G., Homeier, D., & Steffen, M. 2010, A&A, 513, A19
Heinze, A. N., Metchev, S., Apai, D., et al. 2013, ApJ, 767, 173
Helling, C., Ackerman, A., Allard, F., et al. 2008a, MNRAS, 391, 1854
Helling, C., Dehn, M., Woitke, P., & Hauschildt, P. H. 2008b, ApJL, 675, L105
Kaasalainen, M., Torppa, J., & Muinonen, K. 2001, Icar, 153, 37
Kaasalainen, M., & Viikinkoski, M. 2012, A&A, 543, A97
Khandrika, H., Burgasser, A. J., Melis, C., et al. 2013, AJ, 145, 71
Kirkpatrick, J. D. 2005, ARA&A, 43, 195
Knutson, H. A., Charbonneau, D., Allen, L. E., et al. 2007, Natur, 447, 183
Kostov, V. B., & Apai, D. 2012, ApJ, 762, 47
Lafrenière, D., Jayawardhana, R., & van Kerkwijk, M. H. 2008, ApJL, 689, L153
Lagrange, A.-M., Bonnefoy, M., Chauvin, G., et al. 2010, Sci, 329, 57
Leggett, S. K., Geballe, T. R., Fan, X., et al. 2000, ApJL, 536, L35
Looper, D. L., Kirkpatrick, J. D., Cutri, R. M., et al. 2008, ApJ, 686, 528
Lucas, P. W., Roche, P. F., Allard, F., & Hauschildt, P. H. 2001, MNRAS, 326, 695
Lüftinger, T., Fröhlich, H.-E., Weiss, W. W., et al. 2010, A&A, 509, A43
Luhman, K. L., Patten, B. M., Marengo, M., et al. 2007, ApJ, 654, 570
MacKenty, J. W., Kimble, R. A., O'Connell, R. W., & Townsend, J. A. 2010, Proc. SPIE, 7731, 77310
Madhusudhan, N., Burrows, A., & Currie, T. 2011, ApJ, 737, 34
Majeau, C., Agol, E., & Cowan, N. B. 2012, ApJL, 747, L20
Marley, M. S., Fortney, J., Seager, S., & Barman, T. 2007, in Protostars and Planets V, ed. B. Reipurth, D. Jewitt, & K. Keil (Tucson, AZ: Univ. Arizona Press), 733
Marley, M. S., Saumon, D., Cushing, M., et al. 2012, ApJ, 754, 135
Marley, M. S., Saumon, D., & Goldblatt, C. 2010, ApJL, 723, L117
Marois, C., Macintosh, B., Barman, T., et al. 2008, Sci, 322, 1348
Marois, C., Zuckerman, B., Konopacky, Q. M., Macintosh, B., & Barman, T. 2010, Natur, 468, 1080
Metchev, S. A., & Hillenbrand, L. A. 2006, ApJ, 651, 1166
Mohanty, S., Jayawardhana, R., Huélamo, N., & Mamajek, E. 2007, ApJ, 657, 1064
Morley, C. V., Fortney, J. J., Marley, M. S., et al. 2012, ApJ, 756, 172
Patience, J., King, R. R., de Rosa, R. J., & Marois, C. 2010, A&A, 517, A76
Radigan, J., Jayawardhana, R., Lafrenière, D., et al. 2012, ApJ, 750, 105
Radigan, J., Lafrenière, D., Jayawardhana, R., & Doyon, R. 2008, ApJ, 689, 471
Reid, I. N., Cruz, K. L., Kirkpatrick, J. D., et al. 2008, AJ, 136, 1290
Reid, I. N., Lewitus, E., Allen, P. R., Cruz, K. L., & Burgasser, A. J. 2006, AJ, 132, 891
Russell, H. N. 1906, ApJ, 24, 1
Saumon, D., & Marley, M. S. 2008, ApJ, 689, 1327
Showman, A. P., Cho, J. Y.-K., & Menou, K. 2011, in Atmospheric Circulation of Exoplanets, ed. S. Seager (Tucson, AZ: Univ. Arizona Press), 471
Showman, A. P., & Kaspi, Y. 2012, ApJ, submitted (arXiv:1210.7573)
Skemer, A. J., Close, L. M., Szűcs, L., et al. 2011, ApJ, 732, 107
Skemer, A. J., Hinz, P. M., Esposito, S., et al. 2012, ApJ, 753, 14
Snellen, I. A. G., de Kok, R. J., de Mooij, E. J. W., & Albrecht, S. 2010, Natur, 465, 1049
Space Telescope-European Coordinating Facility, ESA 2011, ascl soft, 9016
Tinney, C. G., Burgasser, A. J., & Kirkpatrick, J. D. 2003, AJ, 126, 975
Tsuji, T. 2005, ApJ, 621, 1033
Vogt, S. S., Penrod, G. D., & Hatzes, A. P. 1987, ApJ, 321, 496
Vrba, F. J., Henden, A. A., Luginbuhl, C. B., et al. 2004, AJ, 127, 2948